Biophysical
Reports

ARTICLE

Open-source 3D active sample stabilization for fluorescence microscopy

Sanket Patil,[1,2] Giuseppe Vicidomini,[1] and Eli Slenders[1,*]
[1]Molecular Microscopy and Spectroscopy (MMS), Istituto Italiano di Tecnologia, Genoa, Italy and [2]Department of Informatics, Bioengineering, Robotics and Systems Engineering (DIBRIS), University of Genoa, Genoa, Italy

ABSTRACT Super-resolution microscopy has enabled imaging at nanometer-scale resolution. However, achieving this level of detail without introducing artifacts that could mislead data interpretation requires maintaining sample stability throughout the entire imaging acquisition. This process can range from a few seconds to several hours, particularly when combining live-cell imaging with super-resolution techniques. Here, we present a three-dimensional active sample stabilization system based on real-time tracking of fiducial markers. To ensure broad accessibility, the system is designed using readily available off-the-shelf optical and photonic components. Additionally, the accompanying software is open source and written in Python, facilitating adoption and customization by the community. We achieve a standard deviation of the sample movement within 1 nm in both the lateral and axial directions for a duration in the range of hours. Our approach allows easy integration into existing microscopes, not only making prolonged super-resolution microscopy more accessible but also allowing confocal and widefield live-cell imaging experiments spanning hours or even days.

WHY IT MATTERS Modern microscopes can reveal incredibly small details, but even the tiniest movement—caused by vibrations or temperature changes—can blur an image, making it difficult for scientists to study biological structures at the nanometer scale or perform time-lapse experiments. Our work introduces a new, open-source system that keeps samples stable during long experiments. By tracking gold-nanoparticle markers, our system corrects any shift in three dimensions in real time. Our approach is low cost and easy to integrate into existing custom microscopes, and the software is freely available for researchers worldwide. This innovation will enhance super-resolution and time-lapse microscopy and help scientists capture sharper images of cells and molecules, advancing discoveries in medicine and biology.

INTRODUCTION

Over the past three decades, super-resolution microscopy (SRM) techniques have emerged, enabling a spatial resolution far beyond the diffraction limit (1–5). Notably, in the context of single-molecule localization microscopy (SMLM), resolutions at the Ångström scale have recently been achieved (6–8). SRM opened up the possibility to study cellular processes at the nm scale, allowing, e.g., nanoscale functional topography of chromatin and studying its role in genome integrity (9,10) or observation of structural changes during mitochondria fusion and fission (11). However, the performance of SRM, particularly of SMLM, depends on the inherent stability of the whole imaging system, including the sample. System drift, a pervasive challenge affecting all imaging platforms, significantly hinders the achievable resolution in SRM. This drift arises from a combination of thermal fluctuations and mechanical vibrations within both the imaging system itself and the surrounding environment. The negative impact of system drift becomes evident in the form of a declining image quality ranging from minor imperfections in low-resolution imaging to severe spatial resolution degradation, potential misinterpretation of the data, and even rendering the data unusable in super-resolution applications.

Approaches to address sample drift can be broadly categorized into two methods: active stabilization (12–14) and postprocessing corrections (15–17). Active stabilization focuses on real-time drift correction by continuously monitoring the sample's position, for

---

Submitted January 10, 2025, and accepted for publication April 9, 2025.

*Correspondence: eli.slenders@iit.it

Editor: Jorg Enderlein.

https://doi.org/10.1016/j.bpr.2025.100208

example, by tracking fiducial markers, and by using mechanical or piezoelectric actuators to adjust the sample's position to counteract any drift. This approach can be implemented for all three axes or for axial direction only in scenarios where lateral drift is negligible or addressed through separate corrections (18). Postprocessing corrections address drift after image acquisition. Drift estimation can be achieved either through mathematical model estimation (19) or by imaging fiducial markers alongside the sample (12,14). Notably, without acquiring a full three-dimensional (3D) image stack, axial drift cannot be effectively compensated during postprocessing. Indeed, axial drift leads to out-of-focus images, with inherent information loss as a consequence. Active stabilization is preferred in low-throughput SMLM techniques, such as MINFLUX, RASTMIN, pMINFLUX, and ISM-FLUX (20–24), where the limited number of localized molecules makes it difficult to accurately deduce drift through postprocessing methods.

The use of active stabilization techniques to enhance sample stability has become more widespread in recent years (18,25–28). Additionally, multiple commercial systems with axial stabilization capabilities have emerged (29–31). However, the adaptability of these commercial solutions is often hindered by their limited compatibility with custom-built microscope systems. This has led to the development of numerous custom approaches for sample stabilization, broadly categorized into fiducial-marker-based stabilization and reflection-based stabilization. Fiducial-marker-based stabilization tracks the position of preintroduced fiducial markers, such as gold nanoparticles, gold nanorods, or fluorescent beads, within the sample. Drift is continuously monitored through a dedicated imaging pathway that tracks the position of these markers in real time. Reflection-based stabilization makes use of the reflection of a focused beam off the coverslip. An axial movement of the sample leads to a change in the position or shape of the image of the reflected beam. In both cases, a feedback loop adjusts the sample position to actively compensate for any detected displacement. Each approach presents distinct advantages and limitations. Fiducial-based techniques offer the benefit of 3D stabilization but necessitate the introduction of fiducial markers during sample preparation. Conversely, reflection-based techniques, while requiring no sample alteration, are restricted only to axial correction. Consequently, fiducial-based stabilization strategies are often the preferred choice for low-throughput SMLM methods, such as MINFLUX, which require real-time 3D stabilization.

Several active 3D stabilization systems for custom-built microscopes currently exist (22,24,32). Although these approaches yield stabilization results around 1 nm for all axes, their implementation is either hindered by the need for a costly setup, including a PC with a suitable graphics card for GPU computing; a more complex sample preparation, such as the use of functionalized polystyrene beads; a limited feedback update rate (< 20 Hz); or the lack of open-source availability. Here, we present a fast, open-source 3D active sample stabilization system that delivers similar performance but at a low cost, requiring neither complex sample preparation nor extensive hardware installation. The setup is designed as a modular, standalone add-on that is compact and can be easily integrated with any microscope. Besides the actuators to move the sample, the hardware is based on readily available commercial components, with a total implementation cost around €2500.

MATERIALS AND METHODS

Optical setup and sample

The optical configuration is shown in Fig. 1 *a*. An infrared laser (L780P010: 780 nm, 10 mW, Thorlabs, Newton, New Jersey) serves as the illumination source for the fiducial markers. The collimated beam is split by a 50/50 cube beam splitter (BS014, 700–1100 nm, Thorlabs) and coupled into the microscope with a near-infrared short-pass dichroic mirror (AHF 745/SP BrightLine HC Shortpass Filter, F39-745). By adjusting the mirrors positioned before the beam splitter, the beam is laterally displaced from the optical axis at the back aperture of the objective, leading to highly inclined and laminated optical sheet (HiLo) illumination after passing through the tube lens and objective lens (Nikon Plan Apo VC 100 × /1.40 oil OFN25 DIC N2). The HiLo illumination enables imaging over a large field of view (FOV; $\sim 36 \times 36$ μm), which allows tracking of multiple particles simultaneously to improve robustness and precision (in our experiments, we use a concentration providing a number of particles between 5 and 15). The backscattered signal from the fiducial markers is collected by the same objective and reflected by the near-infrared dichroic mirror to enter the stabilization part again. Here, the beam passes through the 50/50 cube beam splitter and enters a 4f system composed of two lenses, L_1 and L_2 (f $=$ 200 mm each). Both the tube lens and L_1, and L_1 and L_2 form a 4f system. In the conjugate plane between L_1 and L_2, an image of the back focal plane is formed, and the light reflected by the coverslip is focused off axis. An iris diaphragm (IDA25/M, Thorlabs) blocks the light reflected by the coverslip while transmitting most of the backscattered light. Finally, the signal is split with another 50/50 beam splitter and projected onto two CMOS cameras (CS165MU/M - Zelux, Thorlabs), used to independently stabilize the lateral and axial directions, respectively. A cylindrical lens (f $=$ 1000 mm) induces astigmatism into the latter beam path to enable axial position estimation. Using two cameras instead of one effectively prevents aberrations caused by the cylindrical lens from introducing errors in lateral position calculations. The captured images from both cameras are transmitted to a central computer for further processing and calculations. Drift corrections are sent to a three-axis nanopositioning piezoelectric stage (P-545.3R8S PInano, E-727 Controller, Physik Instrumente, Karlsruhe, Germany).

To stabilize the sample, fiducial markers such as gold nanoparticles can be used. Here, we use gold nanoparticles with a diameter ranging from 100 to 150 nm. The choice of gold nanoparticles stems from their several advantageous characteristics: they are

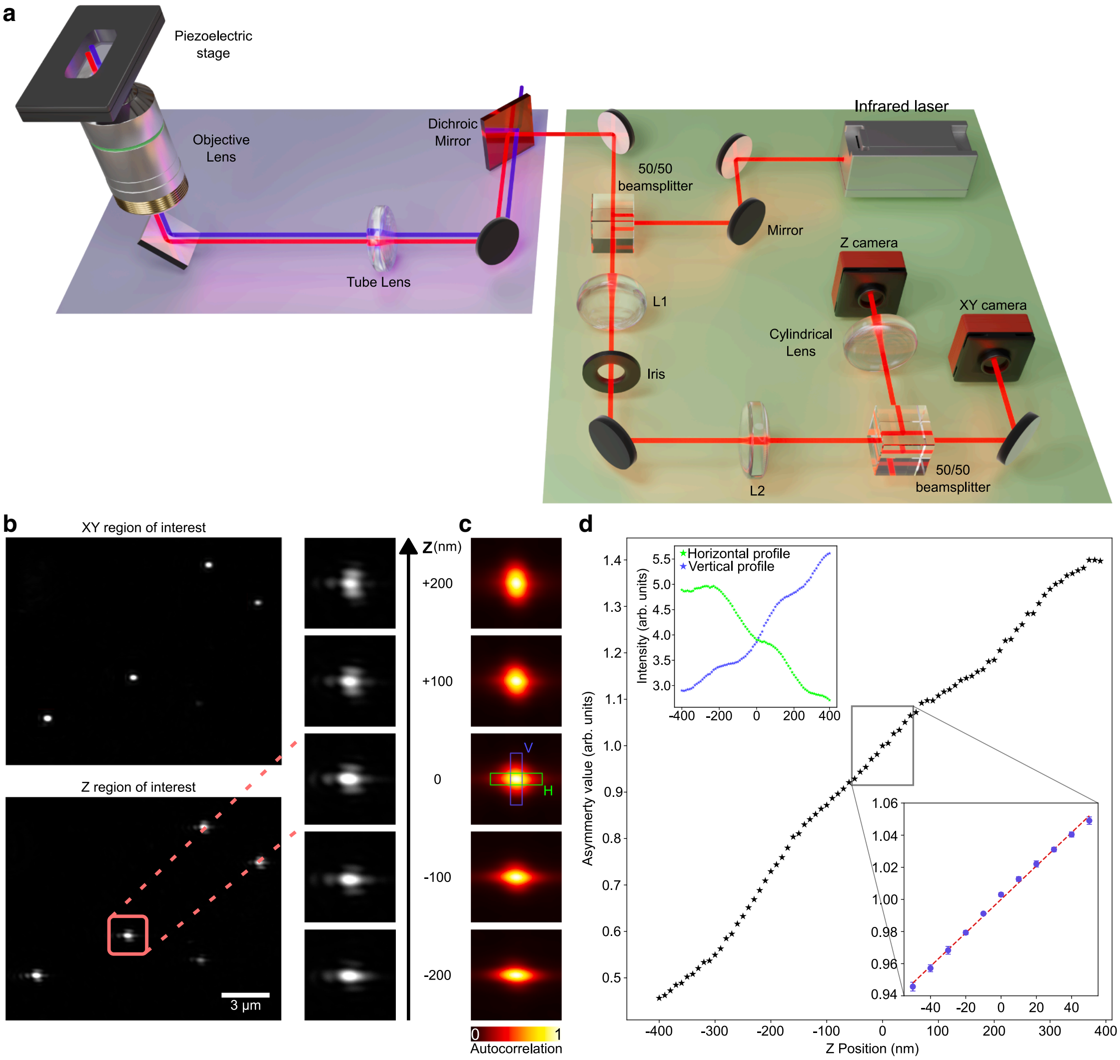

FIGURE 1 Optical setup and axial calibration. (*a*) Optical setup of the stabilization system. The green part shows the stabilization setup, which is coupled to a microscope (partially shown in *purple*). The stabilization beam is coupled into the imaging path using a short-pass dichroic mirror, depicted in red in the imaging part. (*b*) Exemplary camera images of the XY and Z camera. The column on the right shows the astigmatism induced by the cylindrical lens, as imaged by the Z camera at different axial planes. (*c*) Autocorrelation of the images captured by the Z camera for the same *z* positions as in (*b*). The axial position of the sample is derived from the asymmetry of the autocorrelation function, calculated as the ratio of the summed intensities of the pixel values in H (*green*) and V (*blue*). (*d*) Measured autocorrelation asymmetry as a function of the *z* position. The calibration measurement performed at the start of each experiment covers a smaller range (from −50 to +50 nm; *see inset*), where the asymmetry can be well approximated as a linear curve (*dotted line*). The calibration curve and the error bars are the mean and standard deviation over 10 iterations. The inset plot in the top left shows the horizontal and vertical components (shown in *c*) of the summed intensities over the green and blue boxes.

readily available and cost effective at various sizes and capable of scattering laser light across a wide range of wavelengths (33). The components required for building the stabilization are listed in Tables S1 and S2.

Control software

The system integrates a central computer interfacing with the CMOS cameras and the nanopositioning piezoelectric stage. The computer stabilizes the sample by imaging the fiducial markers, performing real-time 3D localization of the particles, and repositioning the stage accordingly. The software is developed in Python and runs entirely on the CPU. We use multiprocessing to parallelize fiducial marker localization in the lateral direction, accelerating drift calculations. The decision to forgo GPU utilization ensures broad compatibility across a diverse range of systems, including systems equipped solely with integrated GPUs or non-NVIDIA-dedicated options, where GPU utilization might not offer a performance advantage and could even impede processing speed due to data transfer overhead.

Before initiating the stabilization process, the software connects to the two CMOS cameras and the nanopositioning piezoelectric stage. All three pieces of hardware require dynamic-link library (.dll) files to establish a connection using the USB 3.0 protocol. These .dll files, provided by the proprietary control software of the cameras (Thorlabs) and the piezoelectric stage (Physik Instrumente), can be installed by the user via a straightforward Windows installation wizard.

After the hardware connection, the user can crop the FOV for each camera independently (Fig. 1 *b*), balancing a larger FOV to capture more particles with a smaller FOV to achieve a higher frame rate. Subsequently, the user selects a chosen number of particles within this FOV for lateral stabilization. The software then performs a *z*-scan using the same piezoelectric stage employed for stabilization to measure the point spread function (PSF) shape at various axial positions (Fig. 1 *b*).

Then, depending on the selected settings, up to 10 processes start running in parallel: one process per camera for image capture, one process per camera for image analysis, one process to control the stage, one process for real-time plotting, and up to four additional processes for miscellaneous tasks, such as data saving, statistical calculations, and data logging. This implementation accommodates processes running at different speeds, allowing the capture of images at a high frame rate (e.g., ~120 Hz), even when stage updates occur at a lower frequency (~20 Hz). Fig. 2 illustrates the pseudocode for the stabilization software and supporting material section A contains more details on the protocol.

Position estimation

We estimate the lateral drift in the camera frame of reference $\boldsymbol{d}(t)$ at time point t by averaging the measured changes in the 2D position of N fiducial markers compared to the start of the measurement: $\boldsymbol{d}(t) = \langle \boldsymbol{x}(t) - \boldsymbol{x}(0) \rangle$, with $\boldsymbol{x}(t)$ representing the positions of the particles at time t. We use the local gradients method (34) to measure $\boldsymbol{x}(t)$ because of its computational efficiency compared to fitting a Gaussian function. Conversion of drift from pixels to nm is done based on a calibration measurement with a reflective grid sample (R1L3S3PR, ThorLabs).

Axial drift estimation is based on astigmatism introduced by the cylindrical lens positioned in front of the camera and comparing the shape of the PSF with respect to the start of the measurement. To estimate the relative z position, we calculate the autocorrelation G in a user-selected region of the image, ideally containing multiple particles for enhanced robustness and precision (Fig. 1, *c* and *d*). We define a measure for the PSF shape A as the ratio $A = \sum_i G_i / \sum_j G_j$ with $i \in V$ and $j \in H$, with H and V perpendicular rectangular regions centered around the autocorrelation peak. Conversion from A to axial displacement in nm is based on a reference curve measured at the start of every measurement (Fig. 1 *d*). This calibration involves sampling multiple planes in both the positive ($+z$) and negative ($-z$) directions with respect to the experiment plane. At each sampled plane, we calculate the corresponding A value. These values are then fitted using linear regression (see the *inset* of Fig. 1 *e*). The slope of the fit represents the conversion factor $\Delta A / \Delta z$, expressed in arbitrary units per nanometer. We typically perform the calibration procedure for a small range (-50 to $+50$ nm) with respect to the initial z position, where the calibration curve can be well approximated by a linear curve. Supporting material section B contains more details on the expected axial localization uncertainty using this method.

RESULTS AND DISCUSSION

First, we measured the performance of the stabilization system using the calculated particle positions

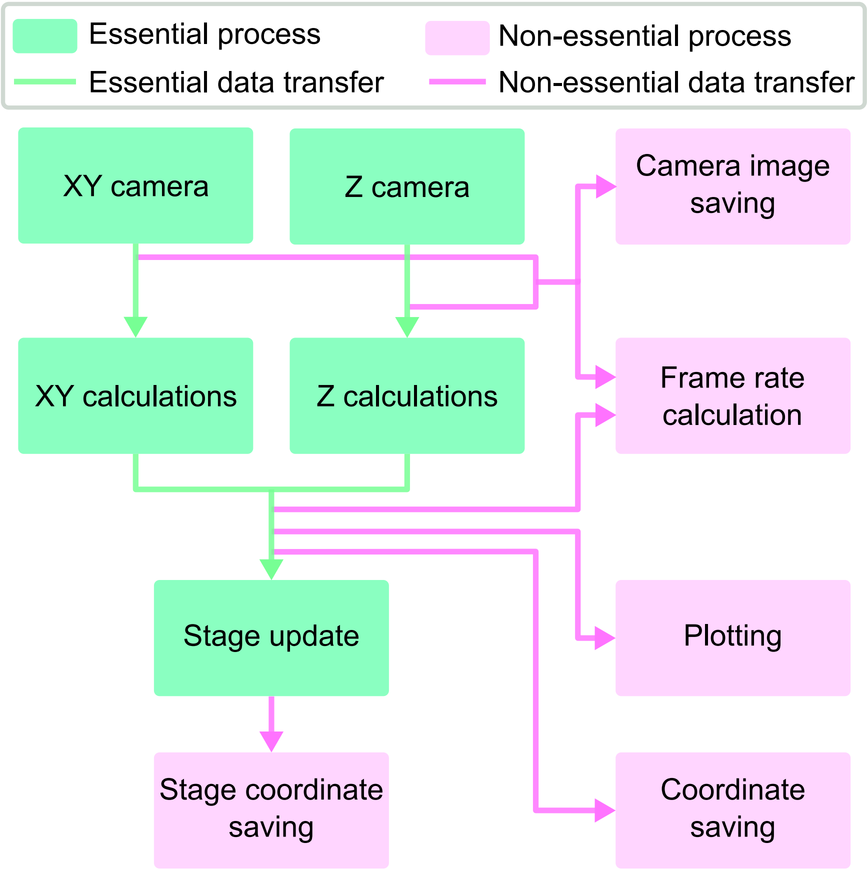

FIGURE 2 Stabilization code workflow. Flowchart with pseudocode describing the stabilization code that controls the hardware. The code is split into 10 different processes that are categorized into two types. The first type (*green*) represents the essential processes required for the stabilization code. The second type (*pink*) represents the nonessential part of the stabilization code. Similarly, the green arrows show essential data transfer, and the pink arrows show nonessential data transfer.

with respect to the start of the measurement in the camera frame of reference, as measured by the stabilization system itself during closed-loop stabilization (Fig. 3 *a*). For all axes, we found a normal distribution with a mean position around 0 and a standard deviation below 1 nm for a 1000 s measurement. Since the nanopositioning piezo system has a closed-loop resolution of 1 nm, and our stabilization software uses a 1 nm threshold for stage updates, we cannot expect a better precision. Note that, due to differences in the frame rate of the cameras and the update rate of the stage, the measured drift may be higher than the 1 nm threshold for multiple consecutive frames, as shown in the insets in Fig. 3 *a*. The corresponding stage position (Fig. 3 *b*), shows about 100 and 200 nm drift in the *x* and *y* directions, respectively, and about 150 nm drift in the axial direction over 1000 s. Comparison of the power spectral density curves of the stage and sample position (Fig. 3 *c*) shows that drift and low-frequency vibrations are suppressed by the stabilization software by more than one order of magnitude in all dimensions. The repositioning of the stage amplifies some vibrations, as can be seen around 1 Hz for the *x* direction and 2.5 Hz for the *z* direction. However, the amplitudes of these vibrations are low enough to keep the overall sample movement below 1 nm standard deviation in each direction.

As a control measurement, we performed long-term confocal imaging of the gold particle sample with the stabilization system running. Specifically,

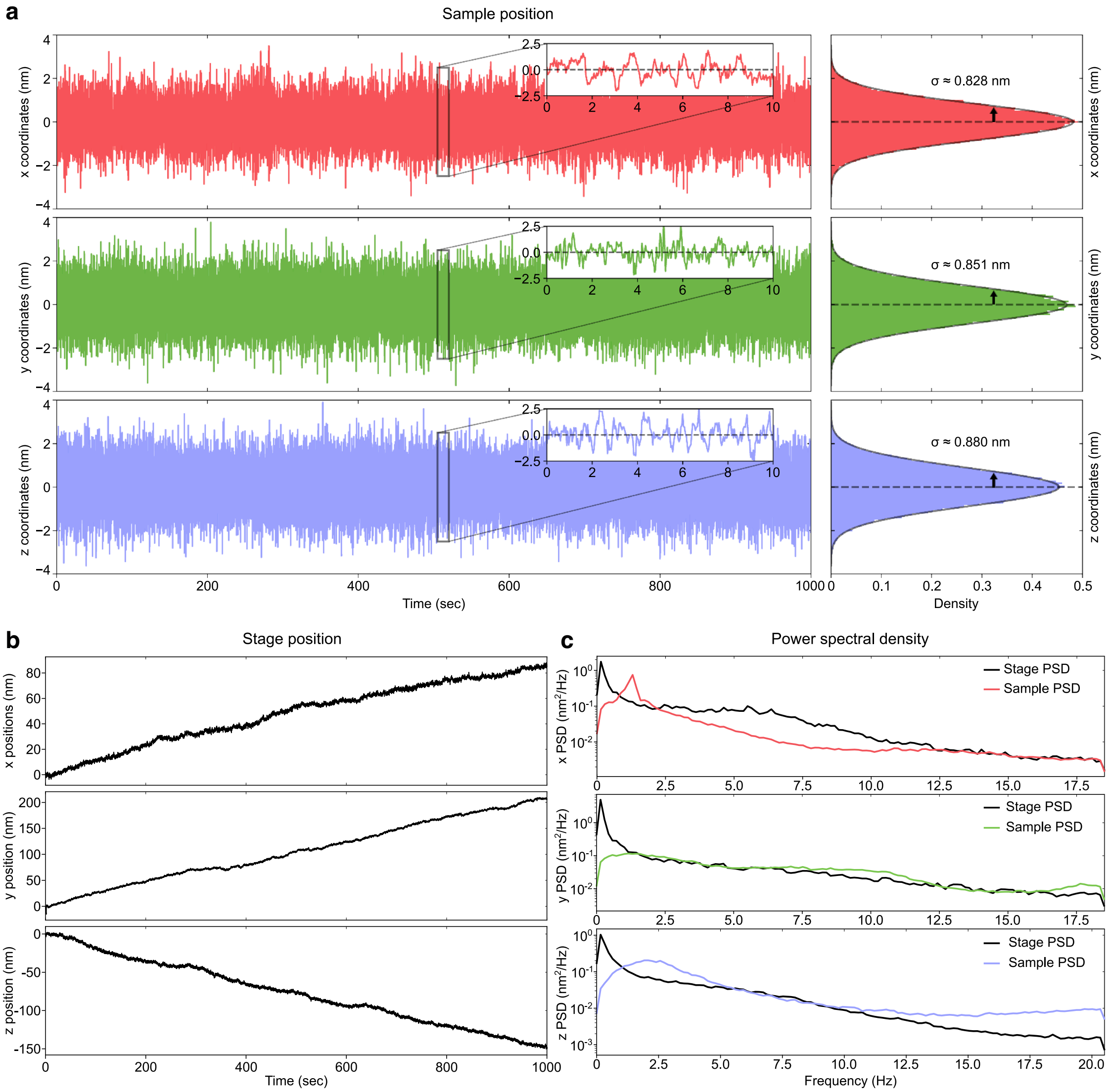

FIGURE 3 Stabilization results. (*a*) Sample position as monitored by the stabilization system and the corresponding histograms showing the distribution of the sample position across time. The parameter σ is the standard deviation of the Gaussian fit to the histogram. (*b*) Corresponding position of the piezoelectric stage for each axis. (*c*) Power spectral density (PSD) of the stabilized sample position (*colored*) and the stage position (*black*).

we removed the band-pass filter from our custom confocal and image scanning microscope to record reflection images in descanned mode using a single-photon avalanche diode array detector (35). Subsequently, we conducted time-series experiments utilizing our microscope control software, BrightEyes-MCS (36). We calculated the lateral drift in the confocal images by phase correlating each image with a reference image taken at the start of the measurement. With the stabilization software running, we observed drifts of (−0.8 ± 1.2) and (−0.6 ± 0.9) nm (mean ± standard deviation) in the *x* and *y* directions, respectively, over the course of 4 h. Although these values exceed the sub-nm precision calculated by the stabilization system, these results may be expected given the additional uncertainty introduced by the galvanometric scan system or other drift components in sections of the beam path that are not common with the stabilization path. With the stabilization system turned off, we measured a lateral drift of more than 500 nm on the *x* axis and more than 900 nm on the *y* axis, with additional drift in the axial direction, moving the sample out of focus (Fig. 4, *b* and *d*).

For both lateral and axial drift calculations, we prioritized lightweight algorithms over slower, more precise alternatives (34). Consequently, the update speed of our system is not limited by the software but by the rate at which the piezo stage controller can process movement commands, here 20 Hz for

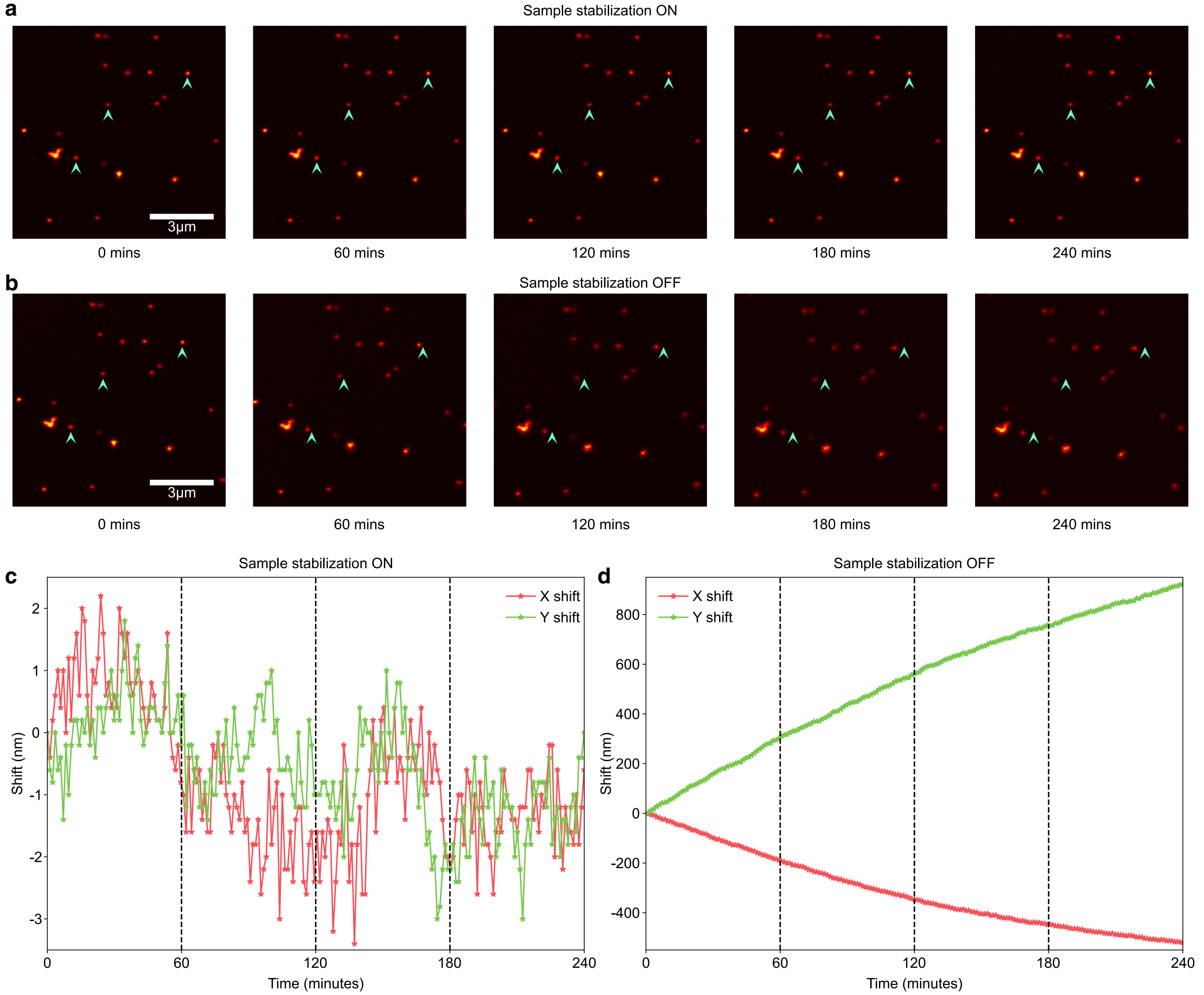

FIGURE 4 Confocal images acquired with and without active stabilization. (*a*) Subset of a time series taken with the active stabilization on. The sample consisted of gold nanoparticles attached to the coverslip surface. Images were acquired every minute for 4 h. With the stabilization system on, there is no visible drift. (*b*) The same measurement with the stabilization system off shows a clear drift in both the lateral and axial directions over the course of 4 h (*c* and *d*) Measured drift in each image with respect to the start of the time lapse, calculated by phase correlation, with the stabilization system on (*c*) and off (*d*).

each axis. For applications where speed and accuracy are less critical, such as time-lapse measurements in confocal or widefield microscopy, alternative algorithms may be preferable. For instance, the local gradients method is well suited to sparse particles whose images are radially symmetric. However, for denser particle distributions or larger, nonradially symmetric structures, other methods, such as phase correlation, will perform better. Similarly, when only axial stabilization is required, analyzing the reflection of a beam off a coverslip can be advantageous, as it eliminates the need for fiducial markers in the sample. Although we have not implemented these alternatives here, the open-source code can be easily adapted to accommodate these custom scenarios.

In summary, we present an active 3D stabilization system for microscopy imaging, utilizing real-time monitoring of infrared back scattering from fiducial markers within the sample. We capture and analyze widefield images at a rate of about 60 Hz and update the stage position at a rate of 20 Hz. In contrast to some earlier methods, our system benefits from parallel processing, enabling significantly faster image acquisition and drift correction. This allows for a more rapid response to sample movement and enhances the overall system stability. The 20 Hz limit in our system is not an inherent restriction of the software but rather a limitation imposed by the digital communication protocol of the piezoelectric stage used in this setup. Our approach yields subnanometer precision across all three spatial dimensions for several hours. The optical system is compact and portable, facilitating easy installation and transfer between different microscopes. The software is open source and runs entirely on the CPU, removing the need for specialized hardware, such as a high-end, GPU-equipped computer. We anticipate that these advantages will make SRM, as well as time-lapse confocal and widefield microscopy experiments, more accessible.

DATA AND CODE AVAILABILITY

The Python code has been deposited on GitHub: https://github.com/VicidominiLab/Active_stabilization.

ACKNOWLEDGMENTS

This research was supported by the European Research Council: BrightEyes no. 818699 (S.P., G.V., and E.S.); the European Union's Horizon 2020 research and innovation programme under the Marie Sklodowska-Curie grant agreement no. 890923 (SMSPAD) (G.V. and E.S.); the NextGeneration EU PNRR MUR—M4C2—Action 1.4—Call Potenziamento strutture di ricerca e creazione di "campioni nazionali di R&S" (CUP J33C22001130001), "National Center for Gene Therapy and Drugs based on RNA Technology," no. CN00000041 (G.V.); and the NQSTI within PNRR MUR project PE0000023-NQSTI (G.V.).

AUTHOR CONTRIBUTIONS

G.V., E.S., and S.P. conceived the idea. E.S. and S.P. built the setup and performed the experiments. G.V., E.S., and S.P. analyzed the data. E.S. and S.P. prepared the samples and wrote the code for the stabilization software. All authors contributed to the writing.

DECLARATION OF INTERESTS

The authors declare that they have no known competing financial interests or personal relationships that could have appeared to influence the work reported in this paper.

SUPPORTING MATERIAL

Supplemental information can be found online at https://doi.org/10.1016/j.bpr.2025.100208.

REFERENCES

1. Gustafsson, M. G. L. 2000. Surpassing the lateral resolution limit by a factor of two using structured illumination microscopy. *J. Microsc.* 198:82–87. https://doi.org/10.1046/j.1365-2818.2000.00710.x.
2. Rust, M. J., M. Bates, and X. Zhuang. 2006. Sub-diffraction-limit imaging by stochastic optical reconstruction microscopy (STORM). *Nat. Methods.* 3:793–795. https://doi.org/10.1038/nmeth929.
3. Betzig, E., G. H. Patterson, ..., H. F. Hess. 2006. Imaging Intracellular Fluorescent Proteins at Nanometer Resolution. *Science.* 313:1642–1645. https://doi.org/10.1126/science.1127344.
4. Hell, S. W., and J. Wichmann. 1994. Breaking the diffraction resolution limit by stimulated emission: stimulated-emission-depletion fluorescence microscopy. *Opt. Lett.* 19:780–782. https://doi.org/10.1364/OL.19.000780.
5. Heilemann, M., S. van de Linde, ..., M. Sauer. 2008. Subdiffraction-resolution fluorescence imaging with conventional fluorescent probes. *Angew. Chem. Int. Ed.* 47:6172–6178.
6. Weber, M., H. von der Emde, ..., S. W. Hell. 2023. MINSTED nanoscopy enters the Ångström localization range. *Nat. Biotechnol.* 41:569–576. https://doi.org/10.1038/s41587-022-01519-4.
7. Weber, M., M. Leutenegger, ..., S. W. Hell. 2021. MINSTED fluorescence localization and nanoscopy. *Nat. Photonics.* 15:361–366. https://doi.org/10.1038/s41566-021-00774-2.
8. Reinhardt, S. C. M., L. A. Masullo, ..., R. Jungmann. 2023. Ångström-resolution fluorescence microscopy. *Nature.* 617:711–716. https://doi.org/10.1038/s41586-023-05925-9.
9. Ochs, F., G. Karemore, ..., C. Lukas. 2019. Stabilization of chromatin topology safeguards genome integrity. *Nature.* 574:571–574. https://doi.org/10.1038/s41586-019-1659-4.
10. Miron, E., R. Oldenkamp, ..., L. Schermelleh. 2020. Chromatin arranges in chains of mesoscale domains with nanoscale functional topography independent of cohesin. *Sci. Adv.* 6:eaba8811. https://doi.org/10.1126/sciadv.aba8811.
11. Yang, X., Z. Yang, ..., P. Xi. 2020. Mitochondrial dynamics quantitatively revealed by sted nanoscopy with an enhanced squaraine variant probe. *Nat. Commun.* 11:3699. https://doi.org/10.1038/s41467-020-17546-1.

12. Lee, S. H., M. Baday, ..., P. R. Selvin. 2012. Using fixed fiduciary markers for stage drift correction. *Opt. Express.* 20:12177–12183. https://doi.org/10.1364/OE.20.012177.
13. Mlodzianoski, M. J., J. M. Schreiner, ..., J. Bewersdorf. 2011. Sample drift correction in 3D fluorescence photoactivation localization microscopy. *Opt. Express.* 19:15009–15019. https://doi.org/10.1364/OE.19.015009.
14. McGorty, R., D. Kamiyama, and B. Huang. 2013. Active microscope stabilization in three dimensions using image correlation. *Opt. Nanoscopy.* 2:3. https://doi.org/10.1186/2192-2853-2-3.
15. Han, R., L. Wang, ..., F. Zhang. 2015. Drift correction for single-molecule imaging by molecular constraint field, a distance minimum metric. *BMC Biophys.* 8:1. https://doi.org/10.1186/s13628-014-0015-1.
16. Wang, Y., J. Schnitzbauer, ..., B. Huang. 2014. Localization events-based sample drift correction for localization microscopy with redundant cross-correlation algorithm. *Opt. Express.* 22:15982–15991. https://doi.org/10.1364/OE.22.015982.
17. Geisler, C., T. Hotz, ..., A. Egner. 2012. Drift estimation for single marker switching based imaging schemes. *Opt. Express, OE.* 20:7274–7289. https://doi.org/10.1364/OE.20.007274.
18. Silvestri, L., M. C. Müllenbroich, ..., F. S. Pavone. 2021. Universal autofocus for quantitative volumetric microscopy of whole mouse brains. *Nat. Methods.* 18:953–958. https://doi.org/10.1038/s41592-021-01208-1.
19. Przybylski, A., B. Thiel, ..., M. Bates. 2017. Gpufit: An open-source toolkit for GPU-accelerated curve fitting. *Sci. Rep.* 7:15722. https://doi.org/10.1038/s41598-017-15313-9.
20. Slenders, E., S. Patil, ..., G. Vicidomini. 2024. Array detection enables large localization range for simple and robust minflux. Preprint at bioRxiv. https://doi.org/10.1101/2024.07.08.602588.
21. Balzarotti, F., Y. Eilers, ..., S. W. Hell. 2017. Nanometer resolution imaging and tracking of fluorescent molecules with minimal photon fluxes. *Science.* 355:606–612. https://doi.org/10.1126/science.aak9913.
22. Gwosch, K. C., J. K. Pape, ..., S. W. Hell. 2020. MINFLUX nanoscopy delivers 3D multicolor nanometer resolution in cells. *Nat. Methods.* 17:217–224. https://doi.org/10.1038/s41592-019-0688-0.
23. Masullo, L. A., F. Steiner, ..., F. D. Stefani. 2021. Pulsed Interleaved MINFLUX. *Nano Lett.* 21:840–846. https://doi.org/10.1021/acs.nanolett.0c04600.
24. Masullo, L. A., A. M. Szalai, ..., F. D. Stefani. 2022. An alternative to MINFLUX that enables nanometer resolution in a confocal microscope. *Light Sci. Appl.* 11:199. https://doi.org/10.1038/s41377-022-00896-4.
25. Rahmani, A., T. Cox, ..., A. Ponjavic. 2024. Astigmatism-based active focus stabilisation with universal objective lens compatibility, extended operating range and nanometer precision. *Opt. Express.* 32:13331–13341.
26. Van den Berg, B., R. Van den Eynde, ..., W. Vandenberg. 2020. A modular approach to active focus stabilization for fluorescence microscopy. Preprint at bioRxiv. https://doi.org/10.1101/2020.09.22.308197.
27. Lin, S., Y. He, ..., X.-W. Chen. 2022. Optical Fingerprint of Flat Substrate Surface and Marker-Free Lateral Displacement Detection with Angstrom-Level Precision. *Phys. Rev. Lett.* 129:213201. https://doi.org/10.1103/PhysRevLett.129.213201.
28. Chen, S.-Y., R. Heintzmann, and C. Cremer. 2019. Sample drift estimation method based on speckle patterns formed by backscattered laser light. *Biomed. Opt. Express.* 10:6462–6475. https://doi.org/10.1364/BOE.10.006462.
29. The Nikon Perfect Focus System (PFS), (2022). https://www.microscopyu.com/tutorials/the-nikon-perfect-focus-system-pfs.Nikon'sMicroscopyU.
30. Leica DMI6000 B with Adaptive Focus Control, (2022). https://www.leica-microsystems.com/products/light-microscopes/p/leica-dmi6000-with-adaptive-focus-control/.
31. TruFocus | Z-Drift Compensation System | Olympus LS, (2022). https://www.olympus-lifescience.com/en/microscopes/inverted/ix83/trufocus/.
32. Coelho, S., J. Baek, ..., K. Gaus. 2021. 3D active stabilization for single-molecule imaging. *Nat. Protoc.* 16:497–515. https://doi.org/10.1038/s41596-020-00426-9.
33. Jain, P. K., K. S. Lee, ..., M. A. El-Sayed. 2006. Calculated absorption and scattering properties of gold nanoparticles of different size, shape, and composition: applications in biological imaging and biomedicine. *J. Phys. Chem. B.* 110:7238–7248.
34. Kashchuk, A. V., O. Perederiy, ..., M. Capitanio. 2023. Particle Localization Using Local Gradients and Its Application to Nanometer Stabilization of a Microscope. *ACS Nano.* 17:1344–1354. https://doi.org/10.1021/acsnano.2c09787.
35. Castello, M., G. Tortarolo, ..., G. Vicidomini. 2019. A robust and versatile platform for image scanning microscopy enabling super-resolution flim. *Nat. Methods.* 16:175–178.
36. Donato, M., E. Slenders, ..., G. V. Brighteyes-mcs. 2024. a control software for multichannel scanning microscopy. *J. Open Source Softw.* 9:103.